Nano Research

Open Access

Research Article

Synergistic enhancement of room-temperature NO_2 sensing by Pt nanoclusters and SAW device

Qiming Yang[1,2,§], Jing Jin[1,§] ✉, Anyu Hu[1], Baile Cui[1], Xufeng Xue[1], Yong Liang[1], and Wen Wang[1,2] ✉

[1] *State Key Laboratory of Acoustics, Institute of Acoustics, Chinese Academy of Sciences, Beijing 100190, China*
[2] *University of Chinese Academy of Sciences, Beijing 100190, China*
[§] *Qiming Yang and Jing Jin contributed equally to this work.*

Cite this article: *Nano Research*, **2026**, *19*, 94908693. https://doi.org/10.26599/NR.2026.94908693

ABSTRACT: The detection of nitrogen dioxide (NO_2) at trace levels remains challenging, particularly under ambient conditions where selectivity and rapid response are critical. Existing room-temperature sensors often suffer from slow kinetics and inadequate gas discrimination. To address the need for room-temperature operation, we developed a surface acoustic wave (SAW) sensor functionalized with a platinum nanoclusters/graphene oxide (Pt-NC/GO) film. The ultra-small platinum nanoclusters (~ 2.4 nm) are uniformly dispersed on GO, enhancing both adsorption and charge transfer. The SAW platform then transduces these interactions into measurable signal variations via its acousto-electric coupling and mass loading effect. The optimized sensor exhibits a sensitivity of 45.4 mV/ppm and a low experimentally measured minimum detectable concentration of 0.02 ppm (20 ppb) and a theoretical limit of detection of 6.6 ppb calculated via the 3σ/k method, outperforming pristine GO (10.7 mV/ppm) and Pt nanoparticles/GO (Pt-NP/GO, 16.1 mV/ppm) references. It also achieves fast response/recovery (50.2/104.0 s) and excellent selectivity against common interferents (H_2, NH_3, CH_4). Additionally, the sensor maintains stable operation over 30 days, with less than 10% signal degradation. The superior performance is attributed to the large surface-to-volume ratio and high density of active sites provided by the platinum nanoclusters, which are crucial for enhancing gas interaction and signal transduction. This work provides new insights into noble-metal-modified two-dimensional materials for environmental monitoring.

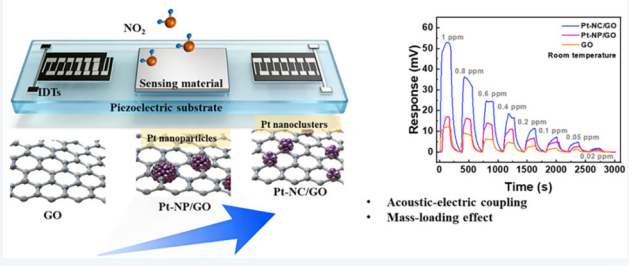

KEYWORDS: surface acoustic wave (SAW) NO_2 sensor, Pt nanoclusters, synergistic effect, trace-level detection, high sensitivity

1 Introduction

With the acceleration of global urbanization and industrialization, nitrogen oxides (NO_x) emissions have become an increasingly severe environmental issue, posing significant threats to human health and ecosystems [1–3]. Among NO_x species, nitrogen dioxide (NO_2) is recognized as the most hazardous due to its strong oxidizing nature and pungent odor. NO_2 can penetrate deep into the lungs, triggering airway inflammation, impairing pulmonary function, and increasing the risk of asthma, cardiovascular diseases, and lung cancer [4–7]. In its 2021 edition of the Global Air Quality Guidelines, the World Health Organization (WHO) significantly lowered the annual mean concentration limit for NO_2 to 10 μg/m^3 (approximately 5.3 ppb), down from the previous threshold of 82 ppb, highlighting increasing concern over the health effects of low-dose NO_2 exposure [8–10]. Due to its high reactivity and complex diffusion behavior, accurate and real-time monitoring of NO_2 concentrations is crucial for the early identification of pollution events and effective environmental management. To enable refined pollution control, sensor technologies with low detection limits, high selectivity, and fast response times are urgently needed to meet the stringent demands of trace gas monitoring.

In recent years, various NO_2 sensing technologies have been developed, including metal oxide semiconductor sensors, electrochemical sensors, optical sensors, and surface acoustic wave (SAW) sensors. Among them, metal oxide semiconductor sensors have attracted significant attention due to their low cost and mature fabrication processes [8, 11–20]. For instance, Mane et al. fabricated

Received: January 22, 2026; **Revised:** March 30, 2026
Accepted: March 30, 2026

✉Address correspondence to Wen Wang, wangwenwq@mail.ioa.ac.cn; Jing Jin, jinjing1@mail.ioa.ac.cn

PPy-WO_3 composite nanomaterials via spin-coating, achieving detection of 100 ppm NO_2 at room temperature, although the sensor response degraded by 20% over 20 days [21]. Oosthuizen et al. prepared CuO nanosheets using a hydrothermal method, achieving a minimum detection limit of 1 ppm with a response time of 350 s [22]. These studies reveal that long-term stability and slow response times remain challenges for metal oxide semiconductor sensors. In contrast, SAW sensors, owing to their high quality factor (*Q*), high operational frequency, and exceptional sensitivity to mass changes, offer the capability of stable and rapid detection of low-concentration NO_2 at room temperature [23–27]. This makes SAW sensors promising candidates for next-generation high-performance gas sensing platforms. The sensing principle of SAW gas sensors is dominated by two synergistic effects, namely the acousto-electric coupling effect and the mass loading effect, which jointly contribute to the sensor's signal response. The acousto-electric coupling effect refers to the perturbation of SAW propagation induced by gas adsorption-induced conductivity changes in the sensitive film, which manifests as variations in SAW velocity and acoustic attenuation. Simultaneously, gas adsorption inevitably leads to an increase in the mass of the sensitive film, which also induces SAW velocity changes, this phenomenon is defined as the mass loading effect. The dual-effect mechanism lays the fundamental basis for the design and optimization of high-performance SAW gas sensors for various practical applications. In recent years, SAW sensors have experienced rapid development, as exemplified by sub-second response speeds in hydrogen sensing and ppb-level detection limits for ammonia, among others [28]. However, few reports have been documented on NO_2 sensing.

The sensing performance of SAW devices is critically dependent on the properties of gas-sensitive materials. To enhance selectivity, response speed, and detection limits, the development of high-performance sensing materials with excellent gas recognition capabilities is essential [29–32]. Among various candidates, graphene-based materials—particularly graphene oxide (GO)—have gained significant attention in recent years due to their two-dimensional structure and high specific surface area, offering superior gas adsorption capacity and chemical reactivity. However, conventional graphene-based materials still suffer from limitations in detection selectivity and long-term stability [33]. To address these limitations, researchers have proposed a synergistic strategy of modifying graphene with noble metal nanoparticles (such as Pt, Pd, and Au). This approach leverages the catalytic activity and electronic sensitization effect of noble metals to enhance the adsorption of target gases. For instance, Bu et al. introduced Pt nanoclusters into ZnO nanowires, reducing the detection limit to 20 ppb [34]. However, their resistive sensor required an elevated operating temperature of 125 °C and exhibited relatively slow response/recovery kinetics (215/378 s). The advantages of platinum nanoclusters (Pt-NC) over nanoparticles (Pt-NP) are attributed to their minimized dimensions, which lead to a high dispersion that maximizes surface atom availability and a quantum size effect that boosts adsorption affinity. The synergistic effect of these factors results in a more optimized NO_2 adsorption energy. Despite these merits, the integration of such highly active Pt-NCs with a low-power, high-sensitivity transduction platform like SAW for room-temperature, rapid NO_2 sensing remains unexplored.

In this work, we present a high-performance, room-temperature NO_2 sensor by integrating platinum nanoclusters with graphene oxide (Pt-NC/GO) as the sensing layer on a SAW device. Uniform Pt nanoclusters (~ 2.4 nm) were anchored on GO, which synergistically enhanced NO_2 adsorption, catalytic activation, and charge transfer. The fabricated sensor exhibits a high sensitivity of 45.4 mV/ppm, rapid response/recovery times of 50.2/104.0 s, and an ultralow detection limit of 0.02 ppm. These enhancements stem from the unique synergy between the atom-efficient Pt nanoclusters (offering maximized active sites) and the sensitive SAW platform, which leverages acousto-electric coupling and mass loading effects to transduce molecular interactions efficiently.

2 Experimental section

2.1 Reagents

All chemical reagents were of analytical grade and used as received without further purification. GO was synthesized via a modified Hummers' method [35]. Hydroiodic acid (HI, 55 wt.%), hydrogen hexachloroplatinate(IV) hexahydrate ($H_2PtCl_6{\cdot}6H_2O$), sodium citrate, and sodium hydroxide (NaOH) were purchased from Sigma-Aldrich.

2.2 Synthesis of Pt-NC/GO and Pt-NP/GO

Few-layer GO was first prepared by reduction and exfoliation. A GO dispersion (0.5 mg/mL) was mixed with HI in a volume ratio of 1:3 and refluxed at 95 °C for 1 h. The resulting precipitate was collected by centrifugation at 3000 rpm for 15 min, washed three times with an ethanol/water mixture (1:1, v/v), and vacuum-dried at 60 °C for 6 h. The obtained GO was redispersed in deionized water at a concentration of 0.1 mg/mL and subjected to ultrasonication for 30 min to achieve a homogeneous suspension. Two composite materials with different Pt loadings were synthesized by adding different volumes of 1 mM H_2PtCl_6 solution. Pt-NC/GO was prepared using a Pt:GO mass ratio of 1:100 (0.8 wt.% Pt), while Pt-NP/GO was synthesized with a higher Pt:GO mass ratio of 1:10 (6.5 wt.% Pt). In both cases, 0.1 M sodium citrate was added as a reducing agent and stabilizer, and the pH was adjusted to 9–10 using 0.05 M NaOH. The reduction was carried out in a microwave reactor operated at 300 W and 80 °C for 2 min. The final products were collected by centrifugation, washed thoroughly with water and ethanol, and dried at 60 °C overnight.

2.3 Fabrication of SAW sensors

A delay-line SAW device was fabricated on a Y35°X-cut quartz piezoelectric substrate. Two aluminum interdigital transducers (IDT) were patterned by photolithography, with a center-to-center distance of 2 mm and a thickness of 120 nm. The input IDT adopted a single-phase unidirectional transducer (SPUDT) structure to reduce insertion loss. The device operated at a fundamental frequency of 200 MHz (wavelength λ = 15.7 μm), with SPUDT electrode widths of 4 μm (λ/4) and 2 μm (λ/8). A 40 nm SiO_2 layer was subsequently sputtered over the IDTs as a passivation layer. The Pt-NC/GO (or Pt-NP/GO) dispersion (0.1 mg/mL in water) was drop-coated onto the delay-line region between the IDT, spread uniformly by low-speed spin-coating (500 rpm, 10 s), and then dried at 60 °C under vacuum for 2 h to form a continuous sensing film.

2.4 Characterization

The morphology, microstructure, and elemental distribution of the composites were examined by high-resolution transmission

electron microscopy (HRTEM, JEOL JEM-2200FS) equipped with energy-dispersive X-ray spectroscopy (EDS). Raman spectra were recorded using a Renishaw in Via spectrometer with a 532 nm laser. Chemical states were analyzed by X-ray photoelectron spectroscopy (XPS, Thermo ESCALAB 250XI, Al Kα source). The SAW device morphology was observed with an optical microscope (OLYMPUS SZ61).

2.5 Gas sensing measurement

The sensing performance was evaluated using a custom phase-detection system (Fig. S1 in the Electronic Supplementary Material (ESM)). A 200 MHz RF signal generated by a network analyzer (Agilent E5061B) excited the SAW device. Phase shifts induced by gas adsorption were monitored through a multi-channel switching module controlled by a microcontroller unit (MCU). The analog signals were digitized by an analog-to-digital converter (ADC) and transmitted to a PC for real-time recording and analysis. NO_2 sensing tests were performed using dynamically mixed gases. Different NO_2 concentrations (0.02–1 ppm) and other gases (H_2, NH_3, CH_4, NO) were prepared by diluting a standard gas/air mixture with high-purity air (99.999%, Shanghai Mingyu Industrial Gas Co., Ltd.) via a gas generator (MF-5B) equipped with mass flow controllers. The total gas flow was maintained at 500 mL/min during all measurements. The response time (T_{90}) was defined as the duration to reach 90% of the final phase shift, and the recovery time (T_{10}) was defined as the time for the maximum phase shift response to recover to 10% of the original baseline in air. All tests were conducted under ambient conditions (25 °C, 40% RH).

As shown in Fig. S2 in the ESM, the phase shift ($\Delta\varphi$) induced by NO_2 adsorption on the Pt-NC/GO sensing layer is converted into a millivolt-level analog voltage by the SAW readout circuit, then sampled and quantized into a digital signal by an ADC, processed by a MCU, and transmitted to a PC via USB for data analysis.

3 Result and discussion

3.1 Fabrication of Pt-NC/GO SAW sensors

The SAW sensor developed in this study employs a delay-line configuration as its core sensing platform. It was fabricated on a Y-cut 35°X-rotated quartz piezoelectric substrate. Two sets of Al IDTs, each with a thickness of 120 nm, were patterned via photolithography, spaced 2 mm apart to define the acoustic delay path. To minimize insertion loss and confine acoustic energy propagation, a SPUDT structure was adopted, utilizing internal reflectors for unidirectional wave emission. The device operates at a center frequency of 200 MHz, corresponding to a surface acoustic wavelength (λ) of approximately 15.7 μm. In accordance with the SPUDT design, the electrode widths were set to 4 μm (λ/4) and 2 μm (λ/8). The overall physical dimensions of the SAW chip are 514λ in length and 169λ in width. A Pt-NC/GO nanocomposite film was integrated as the sensing layer along the acoustic propagation path. The film was prepared by drop-casting an uniformly dispersed aqueous suspension of the synthesized nanomaterial onto the delay-line region. After solvent evaporation, a continuous and homogeneous sensitive coating was formed on the substrate surface, as illustrated in Figs. 1(a) and 1(b).

The frequency response of the device was characterized using a vector network analyzer. As shown in Fig. 1(c), the uncoated SAW sensor exhibited an insertion loss of approximately –11 dB at 200 MHz under room-temperature (25 °C) conditions. After deposition of the Pt-NC/GO layer, the insertion loss increased by about 3 dB, which is attributed to additional acoustic attenuation

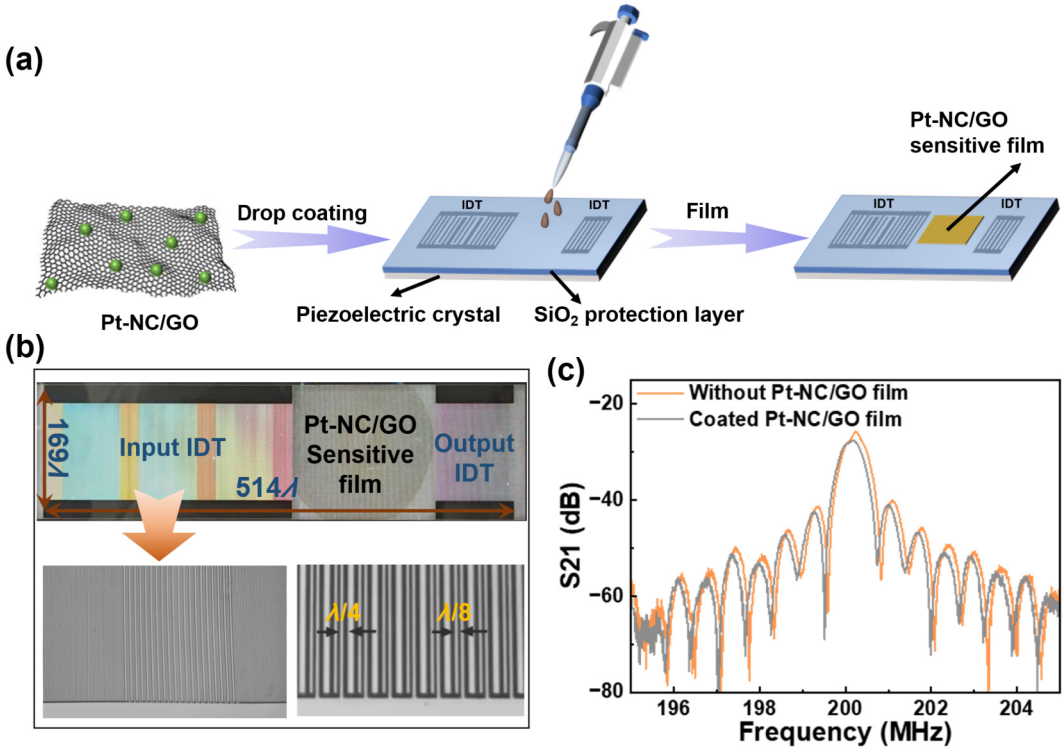

Figure 1 (a) Schematic diagram for the synthesis of the NO_2 SAW sensor with Pt-NC/GO film. (b) Physical drawing of saw nitrogen dioxide sensor device, including SPUDT structure diagram and electrode width of input and output IDT. (c) Frequency response of the SAW NO_2 sensor with/without Pt-NC/GO film at room temperature.

induced by the film. This increase remains within an acceptable range for stable device operation, confirming that the sensitive film does not significantly degrade performance. Moreover, the resulting phase and frequency shifts remain clearly measurable, establishing a reliable basis for subsequent gas sensing experiments.

3.2 Characterization of gas-sensing materials

The Pt-NC/GO composite was synthesized via a facile impregnation-reduction method. This approach was chosen for its mild reaction conditions, operational simplicity, and its capacity to maintain the structural integrity of the GO support, thereby avoiding unintended alterations that could affect the nucleation and uniform dispersion of Pt species. As illustrated in Fig. 2(a), the synthesis began with dispersing GO in deionized water to form a homogeneous suspension, followed by the addition of a chloroplatinic acid precursor. Subsequent *in-situ* reduction at room temperature yielded the final Pt-NC/GO composite.

To elucidate the morphology and dispersion state of the deposited Pt species, systematic transmission electron microscopy (TEM) analyses were conducted. Figure 2(b) showed the typical wrinkled, sheet-like morphology of pristine GO, with no observable particulate features. In contrast, the TEM image of Pt-NC/GO (Fig. 2(c)) revealed numerous bright, high-contrast nanoscale spots uniformly distributed across the GO sheets, confirming the successful loading of Pt at a relatively low loading of 0.8 wt.%. Further high-resolution TEM observation combined with particle-size distribution analysis (Fig. 2(d)) indicated that these spots correspond to ultrafine Pt nanoclusters with a narrow size distribution and an average diameter of approximately 2.4 nm, demonstrating excellent dispersion and structural uniformity. For comparison, the TEM image of the Pt-NP/GO sample with a higher Pt loading of 6.5 wt.% was provided in Fig. S3 in the ESM. In contrast to the well-dispersed nanoclusters in Pt-NC/GO, the Pt-NP/GO composite exhibited significantly larger and more aggregated nanoparticles. This notable difference in particle size and dispersion further highlighted the critical role of the synthesis strategy and Pt loading in controlling the morphology of the metal phase on the GO support.

The Pt-NCs possess an ultrafine average particle size of ~ 2.4 nm, falling well within the typical size range of metal nanoclusters (< 3 nm) [36] and distinct from larger Pt-NPs (> 3 nm). By contrast, the 6.5 wt.% high loading leads to much larger and aggregated Pt particles, which are identified as Pt-NPs.

Following structural characterization, spectroscopic analyses were performed to examine the chemical and surface states of the three samples. First, Raman spectroscopy was used to assess the defect density of GO before and after Pt loading. As shown in Fig. 3(a), all samples displayed characteristic D and G bands near ~ 1350 and ~ 1580 cm^{-1}, respectively. The I_D/I_G ratios were calculated to be 0.98 for pristine GO, 1.01 for Pt-NP/GO, and 1.05 for Pt-NC/GO. The increase in this ratio indicated a rise in defect density after Pt modification. These additional defects likely served as anchoring sites for Pt species and could promote gas adsorption and surface reactions during sensing. Compared with Pt nanoclusters, Pt nanoparticles possessed larger sizes and properties closer to bulk metal. Their interaction with GO was mainly limited

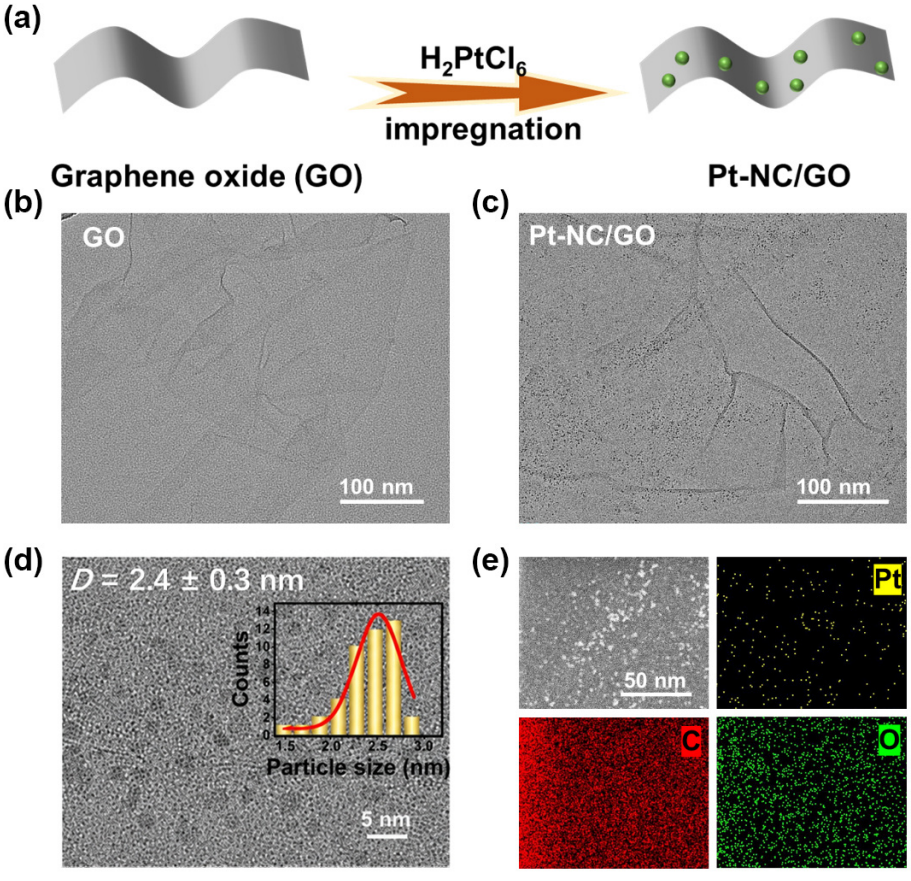

Figure 2 (a) Schematic diagram for the synthesis of Pt-NC/GO. TEM image of (b) GO and (c) Pt-NC/GO. (d) High magnification TEM image and corresponding histograms of the lateral size distributions of Pt-NC/GO. (e) EDX mappings of Pt-NC/GO.

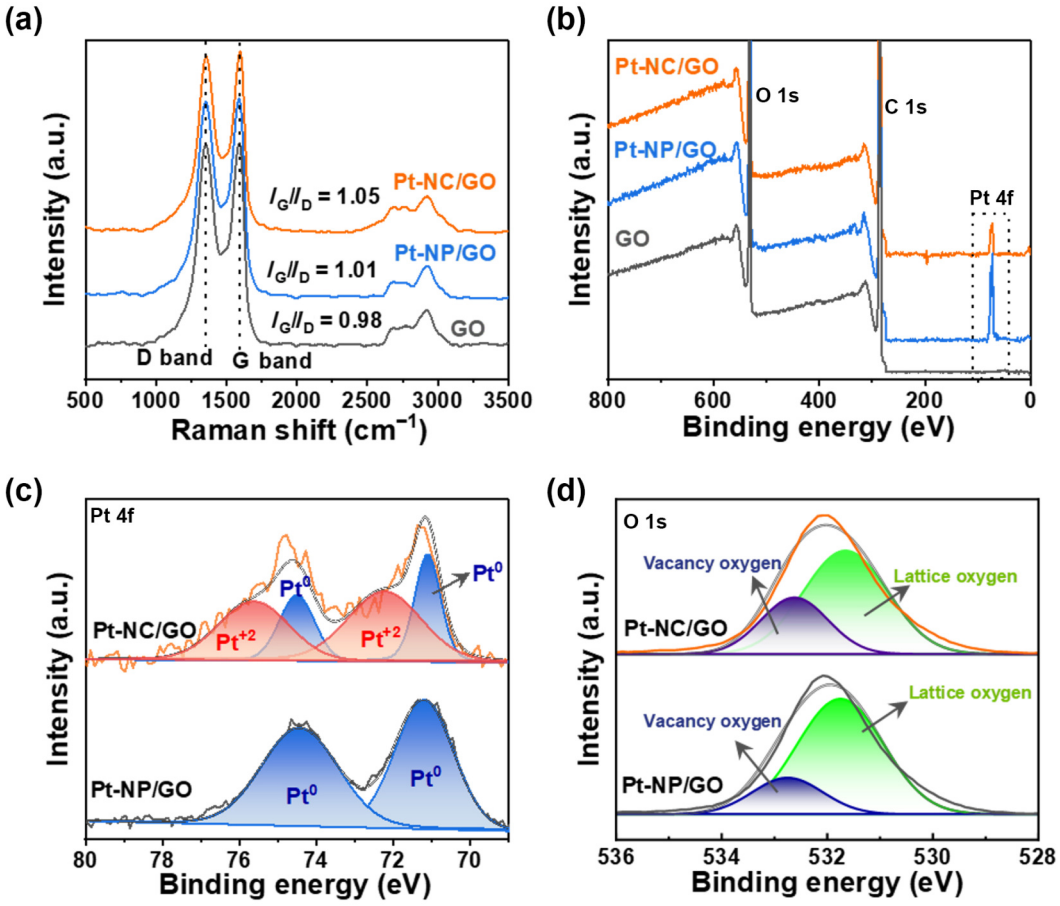

Figure 3 (a) Raman spectrum and (b) XPS survey spectra of Pt-NC/GO, Pt-NP/GO, and GO. (c) Pt 4f and (d) O 1s core level XPS spectra of Pt-NC/GO and Pt-NP/GO.

to interfacial contact, which may have introduced fewer additional defects into the GO structure.

The elemental composition and chemical states were further investigated by XPS. The survey spectra of GO, Pt-NP/GO, and Pt-NC/GO were presented in Fig. 3(b). The GO spectrum showed two predominant peaks corresponding to C 1s (284.6 eV) and O 1s (532 eV). In contrast, both Pt-loaded samples clearly exhibited Pt 4f peaks, confirming the successful incorporation of Pt onto the GO support [37]. High-resolution Pt 4f spectra were then analyzed to compare the chemical states of Pt in the two composites. As displayed in Fig. 3(c), the Pt 4f spectrum of Pt-NC/GO could be deconvoluted into two doublets. The dominant pair at ~ 70.1 eV (Pt $4f_{7/2}$) and ~ 73.4 eV (Pt $4f_{5/2}$) was assigned to metallic Pt^0, while the weaker shoulders at ~ 71.4 and ~ 74.7 eV corresponded to oxidized Pt^{2+} species. The coexistence of Pt^0 and Pt^{2+} indicated the formation of mixed-valence nanoclusters, which can facilitate electron transfer and provide active sites for gas adsorption and surface reactions. In comparison, the Pt 4f spectrum of Pt-NP/GO exhibited only the metallic Pt^0 state, without detectable Pt^{2+} signals. This suggested that the larger Pt nanoparticles behaved more like bulk metal, with less surface oxidation and a weaker electronic interaction with the GO substrate.

The O 1s spectra (Fig. 3(d)) provided further insight into the distribution of oxygen species. Both Pt-NC/GO and Pt-NP/GO showed peaks corresponding to lattice oxygen and oxygen vacancies. Notably, the content of oxygen vacancies was significantly higher in Pt-NC/GO than in Pt-NP/GO. Since oxygen vacancies (e.g., O_2^-, O^-) play a critical role in NO_2 adsorption and dissociation, their lower concentration in Pt-NP/GO directly weakened its ability to capture and activate NO_2 molecules. Two factors may explain this difference: First, the larger Pt nanoparticles in Pt-NP/GO offered a lower density of active sites, reducing the efficiency of O_2 dissociation into active oxygen species; second, the aggregated Pt particles physically covered oxygen-containing functional groups on GO, hindering oxygen adsorption and migration. This also suppressed the oxygen spillover effect from Pt to GO, thereby limiting the generation of additional active sites and slowing the overall NO_2 adsorption-reaction kinetics.

The morphological and spectroscopic results consistently demonstrated the successful synthesis of Pt-NC/GO via an optimized impregnation–reduction approach. This material featured ultrafine, uniformly dispersed Pt nanoclusters, an increased defect density on GO, and stable mixed-valence Pt species—all characteristics that are expected to significantly enhance NO_2 adsorption and sensing performance. Conversely, the XPS comparison indicated that excessive Pt loading in Pt-NP/GO led to particle aggregation, a lower density of active sites, and reduced electron-transfer efficiency, which would likely diminish its NO_2 sensing capability.

3.3 Gas sensing performance

To systematically evaluate the room-temperature NO_2 sensing performance, the dynamic responses of three nanofilms—Pt-NC/GO, Pt-NP/GO, and pure GO—were measured using a SAW device platform at 25 °C. The tests covered NO_2 concentrations from 0.02 to 1 ppm. As shown in Fig. 4(a), the Pt-NC/GO sensor

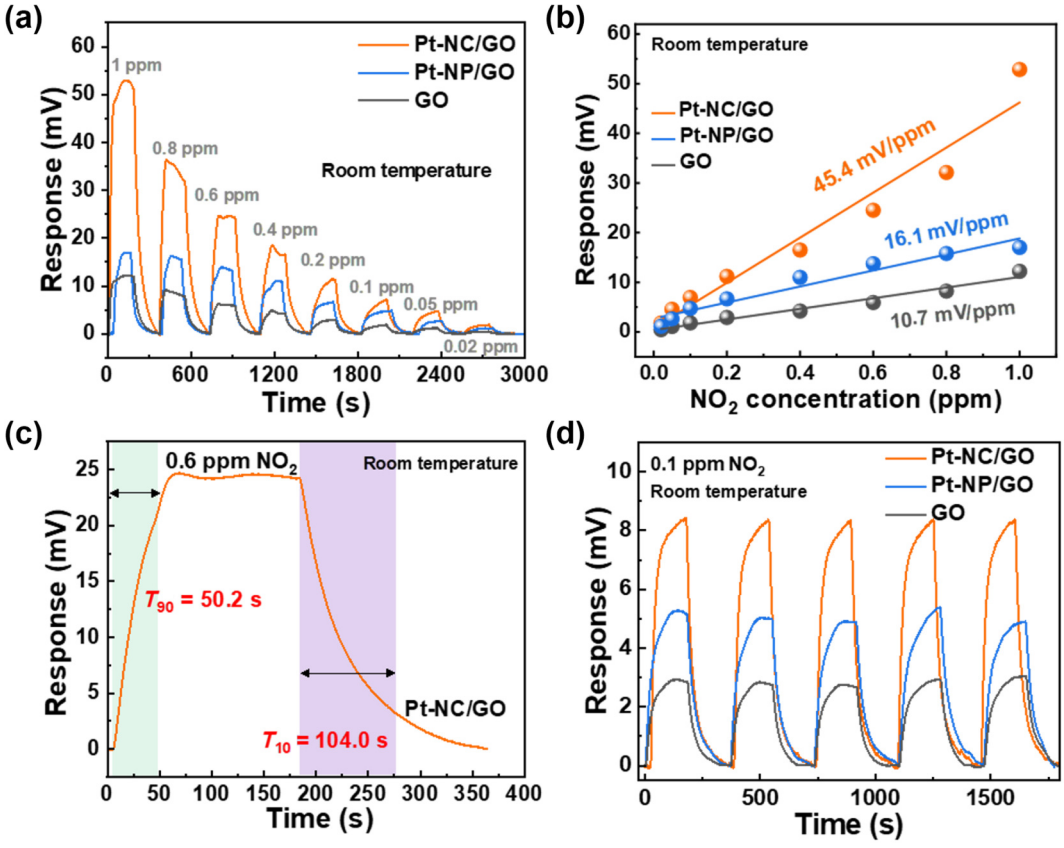

Figure 4 The nitrogen dioxide sensing properties of GO, Pt-NC/GO, Pt-NP/GO. (a) Sensing response, (b) sensitivity, (c) response time and recovery time of Pt-NC/GO to 0.6 ppm NO_2. (d) Repeatability test to 0.1 ppm NO_2.

exhibited a significantly higher response amplitude compared to the other materials. Upon exposure to 1 ppm NO_2, its signal reached 53 mV, which is about 4.4 times greater than that of the pure GO sensor (12 mV). Even at an ultralow concentration of 0.02 ppm, the Pt-NC/GO sensor maintained a discernible response of 1.9 mV, whereas the GO sensor showed only a negligible signal near its detection limit. Sensitivity analysis further confirmed the enhanced sensitivity of the Pt-NC/GO film. As plotted in Fig. 4(b), its sensitivity was calculated to be 45.4 mV/ppm, approximately 4.2 times that of pure GO (10.7 mV/ppm) and 2.8 times that of Pt-NP/GO. This result underscores the critical role of Pt dispersion: Excessive Pt loading in Pt-NP/GO likely induced nanoparticle aggregation and partially covered active sites on GO, thereby reducing the effective surface area for NO_2 interaction. Based on the baseline noise of the SAW readout circuit (≈ 0.1 mV) and using the $3\sigma/k$ method, the theoretical limit of detection (LOD) for the Pt-NC/GO sensor was about 6.6 ppb (where σ is the standard deviation of the baseline noise, k is the sensitivity slope of the sensor at low NO_2 concentrations, k = 45.4 mV/ppm). The response/recovery kinetics were also evaluated. Under 0.6 ppm NO_2, the Pt-NC/GO sensor achieved a T_{90} response time of 50.2 s, notably shorter than that of Pt-NP/GO (58.8 s, Fig. S4(a) in the ESM) and GO (60.2, Fig. S4(b) in the ESM), while its recovery time was 104.0 s (Fig. 4(c)). These results indicate both rapid adsorption and efficient desorption dynamics. Furthermore, the repeatability and stability of the Pt-NC/GO device were verified through five consecutive exposure cycles to 0.1 ppm NO_2 (Fig. 4(d)). The sensor displayed highly consistent response curves, confirming its reliable operational performance.

The comprehensive performance evaluation revealed that the Pt-NC/GO-based SAW sensor exhibited a linear detection range from 0.02 to 1 ppm at room temperature. Its sensitivity, response speed, and repeatability were significantly superior to those of the pure GO-based device. As summarized in Table 1, the overall performance of this sensor also surpasses most previously reported room-temperature NO_2 sensors based on nanomaterials such as metal oxides and carbon composites.

Following the fundamental sensing performance characterization, the practical application potential of the Pt-NC/GO composite was further assessed by systematically investigating its gas selectivity and long-term stability. Selectivity measurements (Fig. 5(a)) demonstrated that at 0.1 ppm, the Pt-NC/GO sensor responded much more strongly to NO_2 than to interfering gases (H_2, NH_3, CH_4, C_2H_2, NO). Although H_2 produced the highest interfering signal (1.9 mV), it remained markedly lower than the response to NO_2 (> 6.9 mV). By contrast, the pure GO sensor showed comparable responses to H_2 and NO_2, indicating poor discrimination. The enhanced selectivity of the Pt-NC/GO sensor is primarily ascribed to the specific adsorption behavior of Pt nanoclusters toward NO_2: Quantum-size effects upshift the d-band center, promoting stronger Pt–NO_2 orbital hybridization, while the sub-nanometer cluster geometry suppresses competing catalytic pathways such as H_2 dissociation.

In terms of operational stability, the sensor retained 90.5% of its initial response after 30 days of storage at 25 °C when exposed to 0.1 ppm NO_2 (Fig. 5(b)). Overall, the Pt-NC/GO material combines high selectivity—particularly against H_2 interference—with excellent long-term stability (monthly decay < 10 %), offering a

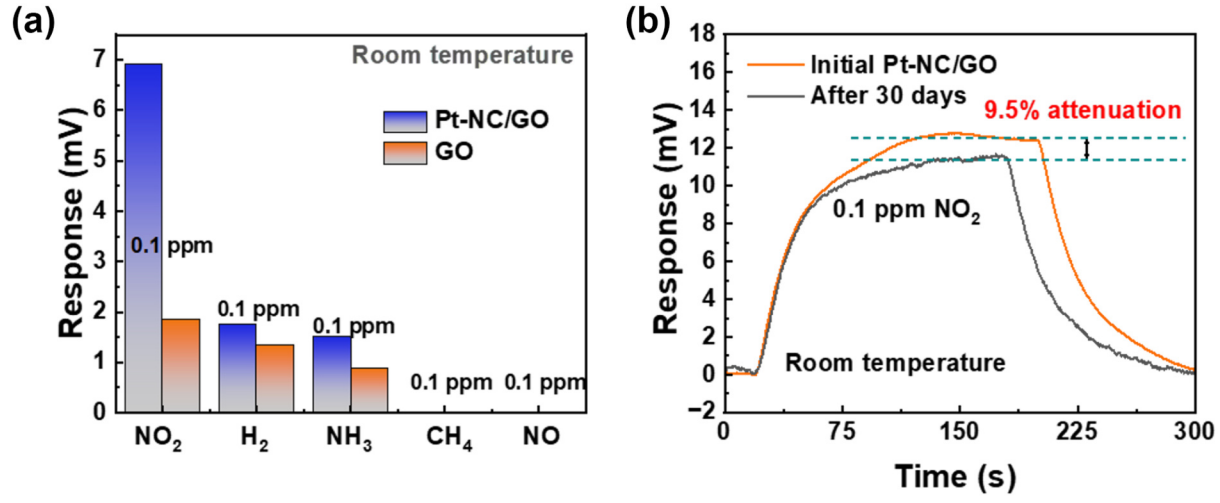

Figure 5 (a) Sensor selectivity for 0.1 ppm NO_2 and 0.1 ppm of other gases at room temperature (25 °C). (b) The sensor response curve of Pt-NC/GO towards 0.1 ppm NO_2 before and after 30 days.

robust material platform for the development of practical room-temperature NO_2 sensors.

Concerning the influence of humidity, the Pt-NC/GO sensing layer exhibited a pronounced humidity dependence due to the presence of GO. The abundant oxygen-containing functional groups on GO readily adsorb water molecules, which alters the electrical conductivity of the composite and introduces noticeable fluctuations in the sensing signal [38, 39]. As demonstrated in Fig. 6, the response of the sensor to nitrogen dioxide was strongly modulated by ambient humidity, confirming the humidity-sensitive character of the Pt-NC/GO system. To address this issue in future work, two main strategies can be pursued. One approach involves the use of humidity-compensation algorithms, where both the sensor output and the ambient humidity are recorded simultaneously. By establishing a quantitative relationship, for example, through multivariate regression or polynomial fitting—the humidity-induced contribution can be subtracted in real time, thereby reducing cross-sensitivity and improving signal stability under varying humidity conditions. Another direction is the development of new material designs with enhanced humidity resistance, such as surface functionalization or incorporation of hydrophobic components. These efforts are expected to further improve the reliability and accuracy of Pt-NC/GO-based sensors in practical environments.

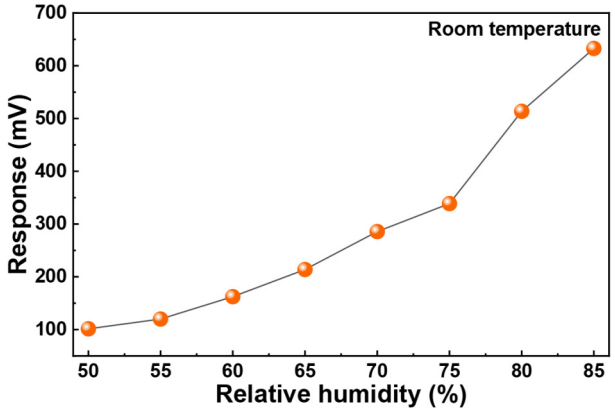

Figure 6 Effect of humidity on nitrogen dioxide sensor at room temperature (25 °C).

Table 1 Comparison of NO_2 sensing performance of nanomaterials-based gas sensor

Materials	Temperature (°C)	Sensing mechanism	Limit of detection	Response/ recovery time (s)	Ref.
CuO nanosheet	25	MOS	1 ppm	350/180	[22]
BP &ZnO nanowire	25	MOS	50 ppb	20/25	[40]
$Ti_3C_2T_x/WS_2$	25	MOS	100 ppb	50/110	[41]
ZnO/ SnO_2@GO	25	MOS	200 ppb	33/92	[42]
Co_3O_4 doped Ce	50	MOS	4.5 ppm	130/2600	[43]
Pt_c-ZnO	125	MOS	20 ppb	215/378	[34]
ZnO film	175	MOS	10 ppm	1200/1800	[44]
Pd-AlGaN/ GaN	300	MOS	100 ppm	120/—	[45]
Pt-NC/GO	25	SAW	20 ppb	50.2/104.0	This work

3.4 Sensing mechanism

3.4.1 High sensitivity mechanism

The sensing mechanism of the Pt-NC/GO composite for nitrogen dioxide (NO_2) relies mainly on the synergistic effects of surface adsorption, electron transfer, and catalytic activation.

GO provided abundant oxygen-containing functional groups, such as hydroxyl, carboxyl, and epoxy groups, which interacted with NO_2 through hydrogen bonding, electrostatic forces, and chemical adsorption. These interactions significantly enhanced the adsorption capacity of the material. In addition, the π-conjugated network of GO engaged in π–π stacking and van der Waals interactions with the π-electron cloud of NO_2, further promoting the initial capture of gas molecules on the surface. The heterogeneous distribution of oxygen functional groups across GO further intensified local adsorption, facilitating the efficient accumulation of NO_2.

Following adsorption, NO_2 acted as a strong oxidizing agent and extracted electrons from the GO framework. This process reduced

the carrier concentration in GO and led to a marked increase in electrical resistance. The associated electron transfer could be described by the following surface reactions

$$O_2 + e^- \rightarrow O_2^- \quad (1)$$

$$2NO_2 + O_2^- + e^- \rightarrow 2NO_3^- \quad (2)$$

$$NO_2 + e^- \rightarrow NO_2^- \quad (3)$$

Adsorbed oxygen molecules captured electrons to form reactive oxygen species (O_2^-), which then reacted with NO_2 to produce nitrate species (NO_3^-). NO_2 could also directly accept electrons to form nitrite ions (NO_2^-). Together, these reactions depleted electrons in GO and modulated its conductivity, providing the fundamental electrical signal for sensing.

While GO served as an adsorbent and charge-transfer medium, the incorporation of platinum nanoclusters substantially improved the sensing performance through multiple synergistic effects. First, the high surface energy and abundant unsaturated sites of Pt nanoclusters offered favorable adsorption centers for NO_2, promoting the formation of reactive Pt-NO_2 intermediates. Second, Pt exhibited pronounced catalytic activity toward oxygen, facilitating the conversion of adsorbed O_2 into more reactive oxygen species (e.g., O_2^-, O^-), which accelerated subsequent reactions with NO_2. Third, Pt clusters acted as electron-sensitization centers, enhancing charge transfer between Pt and GO and lowering the activation energy for NO_2 adsorption and reaction. Fourth, the oxygen spillover effect allowed activated oxygen species to migrate from Pt to the GO surface, supplying additional sites for NO_2 interaction.

In SAW sensors, changes in acoustic attenuation and wave velocity are closely related to the sheet conductivity (σ_{sh}) of the sensing layer. Materials with very low or very high conductivity show limited acousto-electric coupling. In contrast, materials with intermediate conductivity exhibit a strong linear dependence of SAW parameters on σ_{sh}. In this work, the intrinsic sheet conductivity of the sensing film was precisely tuned through Pt loading to fall within this sensitive regime, thereby maximizing the response to NO_2 adsorption and enabling high detection sensitivity.

3.4.2 *Fast response mechanism*

The Pt-NC/GO-based NO_2 sensor, fabricated on a SAW delay line, demonstrated a markedly faster response than most semiconductor-based MEMS sensors. This performance advantage originates from the essential difference in their sensing mechanisms. Unlike semiconductor sensors that only rely on conductivity modulation, SAW sensors realize rapid response through the combined action of acousto-electric coupling and mass loading effects.

In semiconductor MEMS NO_2 sensors, the response originates entirely from chemical changes in the sensitive material's conductivity. The process involves NO_2 adsorption, followed by interfacial charge transfer, carrier concentration modulation, and finally a change in electrical resistance. Each step is kinetically limited by molecular diffusion and surface reaction rates, making the overall response speed constrained by the slowest charge-transfer step.

Conversely, the response of the SAW NO_2 sensor arises from the synergy of two effects: acousto-electric coupling and mass loading. The acousto-electric coupling effect promotes the rapid accumulation of NO_2 molecules onto the sensitive film through field-induced drift, significantly accelerating the initial adsorption kinetics [24]. Simultaneously, the strong adsorption of NO_2 onto the Pt nanoclusters introduces a substantial mass change on the SAW propagation path. This mass loading directly and efficiently translates into a measurable shift in the wave's phase or frequency [46]. Together, these mechanisms enable a faster overall response, as the signal transduction relies on direct physical interactions (mass and electric field coupling) rather than on slower, multistep chemical-electronic processes. The combined contribution of these effects can be quantitatively described by relating the observed frequency or phase shift to the mass of adsorbed gas and the induced surface conductivity change. The composite gas-sensing mechanism can be mathematically described by the following equations

$$\begin{cases} \dfrac{\Delta\alpha}{k_0} = \dfrac{K^2}{2}\left(\dfrac{v_R C_s \sigma_{sh}}{{\sigma_{sh}}^2 + (v_R C_s)^2}\right) \\ \dfrac{\Delta v}{v_R} = fh\rho(k_1 + k_2 + k_3) - \dfrac{K^2}{2}\left(\dfrac{{\sigma_{sh}}^2}{{\sigma_{sh}}^2 + (v_R C_s)^2}\right) \end{cases} \quad (4)$$

where $\Delta\alpha$ denotes acoustic attenuation, k_0 is the wave number, K^2 represents the electromechanical coupling coefficient, v_R is the unperturbed SAW velocity, C_s is the unit capacitance of the piezoelectric crystal, σ_{sh} is the sheet conductivity of the sensitive film, Δv is the perturbed SAW velocity, f is the operating frequency, h is the thickness of the sensitive film, ρ is the density of the sensitive film, and k_1, k_2, k_3 are the piezoelectric substrate coupling constants. Notably, acoustic attenuation is exclusively induced by the acousto-electric coupling effect, while the SAW velocity variation is jointly contributed by the mass loading effect (first term) and the acousto-electric coupling effect (second term).

The response mechanism of the Pt-NC/GO-based SAW sensor was governed by the synergistic operation of two parallel effects: acousto-electric coupling and mass loading. This combination established a "mechanical-electrical dual-path" sensing paradigm, which significantly accelerated the overall response.

First, the acousto-electric coupling effect, analogous to that in semiconductor-based MEMS sensors, relied on changes in the electrical conductivity of the sensitive material. Upon exposure to NO_2, electron transfer between NO_2 molecules and the Pt-NC/GO composite altered its sheet conductivity (σ_{sh}), thereby perturbing the propagation of the surface acoustic wave through acousto-electric interaction. This process provided the basis for chemical recognition of NO_2, although its speed was inherently limited by the kinetics of charge transfer.

In contrast, the mass loading effect—a distinctive advantage of SAW sensors—operated independently of electron transfer. As expressed in the relevant equations, the immediate physical adsorption (physisorption) of NO_2 onto the Pt-NC/GO surface increased the areal mass density, which directly modified the SAW velocity via the mass-loading term $(fh\rho(k_1 + k_2 + k_3)$. Being a purely physical process, mass loading produced a rapid signal response without waiting for slow charge-transfer steps.

In practice, the two mechanisms functioned in parallel: The mass-loading effect initiated an immediate response during physisorption, while the acousto-electric coupling effect subsequently reinforced the signal through chemical recognition after charge transfer. As illustrated in Fig. 7, this dual-path mechanism broke the single-path bottleneck typical of conventional MEMS sensors, thereby markedly shortening the overall response

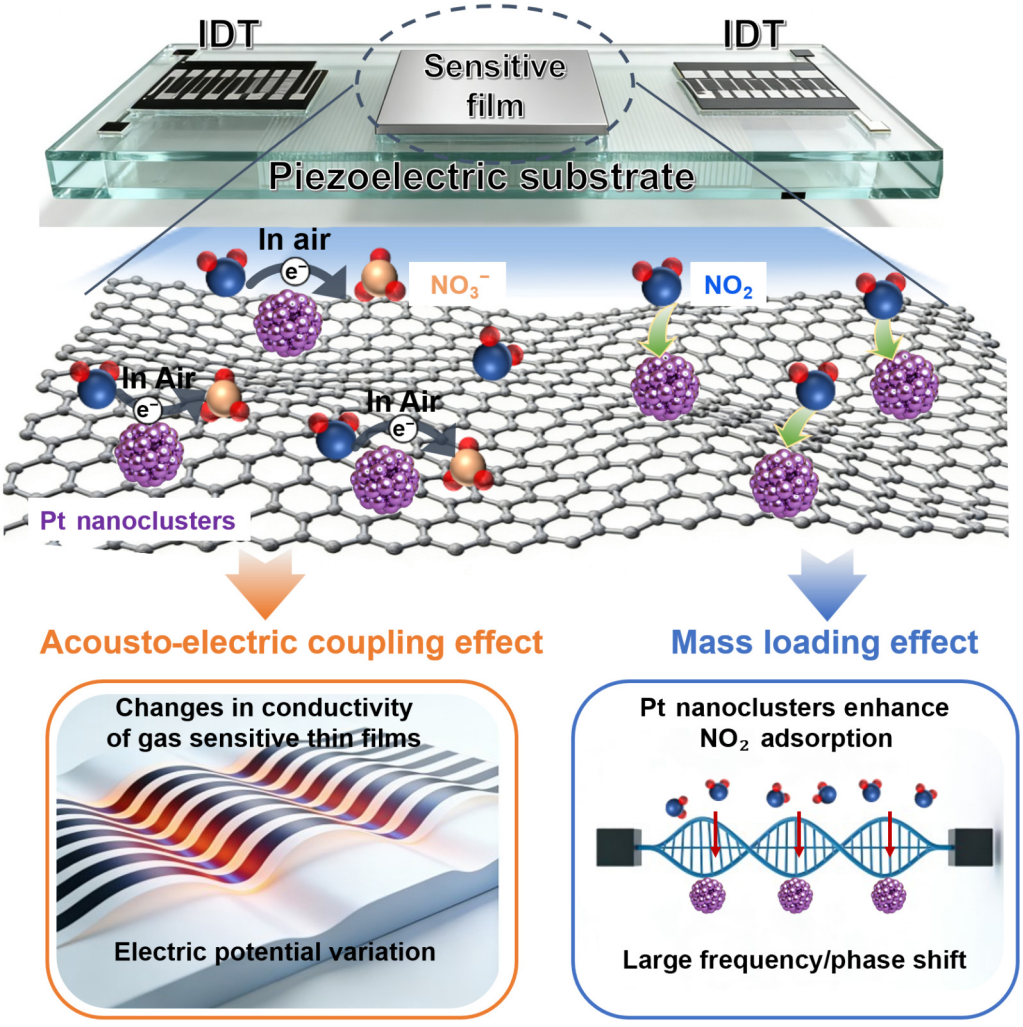

Figure 7 Sensing mechanism of Pt-NC/GO SAW sensor to NO_2.

time through the fast, charge-transfer-independent contribution of mass loading.

In addition to the dual-effect transduction of the SAW sensor that accelerates recovery, ambient water molecules also play a crucial role in promoting the desorption of adsorbed NO_2 species [47]. Water molecules form hydrogen-bonded clusters with NO_2^- and NO_3^- on the Pt-NC/GO surface, reducing the binding energy of these nitrogen-containing species and thus facilitating their rapid dissociation and desorption from active sites, which further ensures the efficient recovery of the sensor in air.

4 Conclusions

In this work, a room-temperature NO_2 SAW sensor based on Pt-NC/GO composite films was developed. The sensor showed high sensitivity (45.4 mV/ppm), fast response/recovery (50.2 s/104.0 s), a low experimentally measured minimum detectable concentration of 0.02 ppm (20 ppb) and a theoretical limit of detection of 6.6 ppb. The enhanced performance stems from the synergy between Pt nanoclusters and the SAW platform. Pt nanoclusters (~ 2.4 nm) provide abundant active sites for NO_2 adsorption and promote charge transfer. Meanwhile, the SAW device utilizes a dual-path mechanism: The mass-loading effect enables rapid physical response, and the acousto-electric coupling effect amplifies the signal through conductivity changes, collectively accelerating the sensing kinetics. The sensor also exhibited excellent selectivity and long-term stability. This study offers an effective strategy for trace-level NO_2 detection and provides insights for designing noble-metal-modified sensing materials. Notably, the sensor exhibits humidity sensitivity in practical applications, which limits its direct use in variable-humidity environments. Future research will focus on humidity compensation strategies and hydrophobic surface modification to enhance environmental adaptability.

Electronic Supplementary Material: Supplementary material (experimental details, characterization results, sensing system configuration, and additional gas sensing data supporting the conclusions of this study) is available in the online version of this article at https://doi.org/10.26599/NR.2026.94908693.

Data availability

All data needed to support the conclusions in the paper are presented in the manuscript and the Electronic Supplementary Material. Additional data related to this paper may be requested from the corresponding author upon request.

Acknowledgements

This work was financially supported by National Key Research and Development Program (No. 2024YFE0199800) and the National Natural Science Foundation of China (No. 12404543).

Declaration of competing interest

The authors declare no conflict of interest.

Author contribution statement

Q. M. Y.: Conceptualization, investigation, writing – original draft, visualization. J. J.: Supervision, resource, writing – review & editing, funding acquisition, project administration. A. Y. H.: Software, validation. B. L. C.: Methodology, data curation. X. F. X.: Literature search, validation. Y. L.: Visualization, formal analysis. W. W.: Supervision, writing – review & editing, funding acquisition.

Use of AI statement

None.

References

[1] Samoli, E.; Aga, E.; Touloumi, G.; Nisiotis, K.; Forsberg, B.; Lefranc, A.; Pekkanen, J.; Wojtyniak, B.; Schindler, C.; Niciu, E. et al. Short-term effects of nitrogen dioxide on mortality: An analysis within the APHEA project. *Eur. Respir. J.* **2006**, *27*, 1129–1138.

[2] Lewné, M.; Cyrys, J.; Meliefste, K.; Hoek, G.; Brauer, M.; Fischer, P.; Gehring, U.; Heinrich, J.; Brunekreef, B.; Bellander, T. Spatial variation in nitrogen dioxide in three European areas. *Sci. Total Environ.* **2004**, *332*, 217–230.

[3] Huang, S. W.; Li, H. M.; Wang, M. R.; Qian, Y. Y.; Steenland, K.; Caudle, W. M.; Liu, Y.; Sarnat, J.; Papatheodorou, S.; Shi, L. H. Long-term exposure to nitrogen dioxide and mortality: A systematic review and meta-analysis. *Sci. Total Environ.* **2021**, *776*, 145968.

[4] Hesterberg, T. W.; Bunn, W. B.; McClellan, R. O.; Hamade, A. K.; Long, C. M.; Valberg, P. A. Critical review of the human data on short-term nitrogen dioxide (NO_2) exposures: Evidence for NO_2 no-effect levels. *Crit. Rev. Toxicol.* **2009**, *39*, 743–781.

[5] Hasselblad, V.; Eddy, D. M.; Kotchmar, D. J. Synthesis of environmental evidence: Nitrogen dioxide epidemiology studies. *J. Air Waste Manage. Assoc.* **1992**, *42*, 662–671.

[6] Hamra, G. B.; Laden, F.; Cohen, A. J.; Raaschou-Nielsen, O.; Brauer, M.; Loomis, D. Lung cancer and exposure to nitrogen dioxide and traffic: A systematic review and meta-analysis. *Environ. Health Perspect.* **2015**, *123*, 1107–1112.

[7] Faustini, A.; Rapp, R.; Forastiere, F. Nitrogen dioxide and mortality: Review and meta-analysis of long-term studies. *Eur. Respir. J.* **2014**, *44*, 744–753.

[8] Fang, H. R.; Shang, E. Y.; Wang, D.; Ma, X.; Zhao, B.; Han, C. S.; Zheng, C. X. A chemiresistive ppt level NO_2 gas sensor based on CeO_2 nanoparticles modified CuO nanosheets operated at 100°C. *Sens. Actuators B: Chem.* **2023**, *393*, 134277.

[9] Devalia, J. L.; Rusznak, C.; Herdman, M. J.; Trigg, C. J.; Davies, R. J.; Tarraf, H. Effect of nitrogen dioxide and sulphur dioxide on airway response of mild asthmatic patients to allergen inhalation. *Lancet* **1994**, *344*, 1668–1671.

[10] Chen, T. M.; Kuschner, W. G.; Gokhale, J.; Shofer, S. Outdoor air pollution: Nitrogen dioxide, sulfur dioxide, and carbon monoxide health effects. *Am. J. Med. Sci.* **2007**, *333*, 249–256.

[11] Jha, R. K.; D'Costa, J. V.; Sakhuja, N.; Bhat, N. $MoSe_2$ nanoflakes based chemiresistive sensors for ppb-level hydrogen sulfide gas detection. *Sens. Actuators B: Chem.* **2019**, *297*, 126687.

[12] Jung, G.; Shin, H.; Jeon, S. W.; Lim, Y. H.; Hong, S.; Kim, D. H.; Lee, J. H. Transducer-aware hydroxy-rich-surface indium oxide gas sensor for low-power and high-sensitivity NO_2 gas sensing. *ACS Appl. Mater. Interfaces* **2023**, *15*, 22651–22661.

[13] Kim, J. H.; Mirzaei, A.; Kim, H. W.; Kim, S. S. Realization of Au-decorated WS_2 nanosheets as low power-consumption and selective gas sensors. *Sens. Actuators B: Chem.* **2019**, *296*, 126659.

[14] Li, L.; He, S. J.; Liu, M. M.; Zhang, C. M.; Chen, W. Three-dimensional mesoporous graphene aerogel-supported SnO_2 nanocrystals for high-performance NO_2 gas sensing at low temperature. *Anal. Chem.* **2015**, *87*, 1638–1645.

[15] Liu, Y. N.; Li, S.; Meng, S. J.; Xiao, S.; Song, H.; Du, K. Defects-enriched two-dimensional ultrathin g-C_3N_4/In_2O_3 nanoparticles for effective NO_2 detection at room temperature. *Sens. Actuators B: Chem.* **2023**, *396*, 134558.

[16] Liu, Y. Y.; Liu, J. J.; Pan, Q. J.; Pan, K.; Zhang, G. Metal-organic framework (MOF) derived In_2O_3 and g-C_3N_4 composite for superior NO_x gas-sensing performance at room temperature. *Sens. Actuators B: Chem.* **2022**, *352*, 131001.

[17] Shen, Y. B.; Li, G. D.; Zhao, S. K.; Bai, J. Z.; Liu, Z. Y.; Cui, B. Y.; Wei, D. Z.; Meng, D.; Meng, F. L. Synthesis of rGO-SnO_2 nanocomposites using GO as an alkali-resistant substrate for high-performance detection of NO_2. *Sens. Actuators B: Chem.* **2023**, *388*, 133804.

[18] Wang, C. Y.; Xie, J. Y.; Chang, X.; Zheng, W.; Zhang, J.; Liu, X. H. ZnO single nanowire gas sensor: A platform to investigate the sensitization of Pt. *Chem. Eng. J.* **2023**, *473*, 145481.

[19] Yang, J. H.; Peng, H. R.; Lin, C.; Pan, Q. J.; Qi, L. X.; Li, L.; Shi, K. Y. UiO-66 metal-organic framework-derived ZrO_2/ZnO mesoporous materials for high-efficiency detection of NO_2 at room temperature. *J. Mater. Chem. A* **2023**, *11*, 22859–22867.

[20] Zhou, W. R.; Han, J. Y.; Kong, D. H.; Gao, Y. B.; Gao, Y.; Wang, Y.; Lu, G. Y. Interfacial oxygen vacancies and energy-level engineering on CeO_2-PPy-rGO nanocomposites towards boosted NO_2 sensor performance. *Sens. Actuators B: Chem.* **2023**, *396*, 134614.

[21] Mane, A. T.; Navale, S. T.; Sen, S.; Aswal, D. K.; Gupta, S. K.; Patil, V. B. Nitrogen dioxide (NO_2) sensing performance of p-polypyrrole/n-tungsten oxide hybrid nanocomposites at room temperature. *Org. Electron.* **2015**, *16*, 195–204.

[22] Oosthuizen, D. N.; Korditis, I.; Swart, H. C.; Motaung, D. E. Facile control of room temperature nitrogen dioxide gas selectivity induced by copper oxide nanoplatelets. *J. Colloid Interface Sci.* **2020**, *560*, 755–768.

[23] Zhou, L. C.; Hu, Z. X.; Wang, P.; Gao, N. B.; Zhai, B. H.; Ouyang, M.; Zhang, G. Z.; Chen, B. B.; Luo, J. T.; Jiang, S. L. et al. Enhanced NO_2 sensitivity of SnO_2 SAW gas sensors by facet engineering. *Sens. Actuators B: Chem.* **2022**, *361*, 131735.

[24] Ricco, A. J.; Martin, S. J.; Zipperian, T. E. Surface acoustic wave gas sensor based on film conductivity changes. *Sens. Actuators* **1985**, *8*, 319–333.

[25] Lec, R.; Vetelino, J. F.; Falconer, R. S.; Xu, A. Macroscopic theory of surface acoustic wave gas microsensors. In *IEEE 1988 Ultrasonics Symposium Proceedings*, Chicago, USA, 1988, pp 585–589.

[26] Devkota, J.; Greve, D. W.; Hong, T.; Kim, K. J.; Ohodnicki, P. R. An 860 MHz wireless surface acoustic wave sensor with a metal-organic framework sensing layer for CO_2 and CH_4. *IEEE Sens. J.* **2020**, *20*, 9740–9747.

[27] Cui, B. L.; Jin, J.; Hu, A. Y.; Ren, Z. X.; Liang, Y.; Wang, W.; Cheng, L. N. Multiphysics coupled sensing mechanism of Pd/Ni alloy thin-film coated SAW hydrogen sensor. *Smart Mater. Struct.* **2024**, *33*, 055009.

[28] Yang, Q. M.; Cui, B. L.; Jin, J.; Cheng, L. N.; Xue, X. F.; Yin, Y. N.; Wang, W. Review of surface acoustic wave-based gas sensors. *Sens. Int.* **2026**, *7*, 100348.

[29] Shen, C. Y.; Cheng, Y. H.; Wang, S. H. A nitrogen dioxide surface acoustic wave sensor based on polyaniline/tungsten oxide nanocomposite. In *2010 International Conference on Measuring*

Technology and Mechatronics Automation, Changsha, China, 2010, pp 204–207.

[30] Lim, C.; Wang, W.; Yang, S.; Lee, K. Development of SAW-based multi-gas sensor for simultaneous detection of CO_2 and NO_2. *Sens. Actuators B: Chem.* **2011**, *154*, 9–16.

[31] Hu, Y. W.; Xiang, J. W.; Sun, X. Y.; Xu, C. Z.; Wang, S.; Duan, J. Sensitivity improvement of SAW NO_2 sensors by p-n heterojunction nanocomposite based on MWNTs skeleton. *IEEE Sens. J.* **2016**, *16*, 287–292.

[32] Ippolito, S. J.; Kandasamy, S.; Kalantar-zadeh, K.; Wlodarski, W.; Galatsis, K.; Kiriakidis, G.; Katsarakis, N.; Suchea, M. Highly sensitive layered ZnO/$LiNbO_3$ SAW device with InO_x selective layer for NO_2 and H_2 gas sensing. *Sens. Actuators B: Chem.* **2005**, *111–112*, 207–212.

[33] Lim, J. B.; Reddeppa, M.; Nam, D.; Pasupuleti, K. S.; Bak, N. H.; Kim, S. G.; Cho, H. D.; Kim, M. D. Surface acoustic device for high response NO_2 gas sensor using *p*-phenylenediamine-reduced graphene oxide nanocomposite coated on langasite. *Smart Mater. Struct.* **2021**, *30*, 095016.

[34] Bu, W. Y.; Zhou, Y.; Liu, N.; Zhang, Y.; Han, W. J.; Chuai, X.; Zhou, Z. J.; Hu, C. H.; Lu, G. Y. ZnO nanowires decorated with Pt nanoclusters for selective detection of ppb-level nitrogen dioxide. *Sens. Actuators B: Chem.* **2024**, *419*, 136391.

[35] Hsieh, S. H.; Hsu, M. C.; Liu, W. L.; Chen, W. J. Study of Pt catalyst on graphene and its application to fuel cell. *Appl. Surf. Sci.* **2013**, *277*, 223–230.

[36] Yao, Q. F.; Zhu, M. S. Q.; Yang, Z. C.; Song, X. R.; Yuan, X.; Zhang, Z. P.; Hu, W. P.; Xie, J. P. Molecule-like synthesis of ligand-protected metal nanoclusters. *Nat. Rev. Mater.* **2025**, *10*, 89–108.

[37] Smirnov, M. Y.; Kalinkin, A. V.; Vovk, E. I.; Simonov, P. A.; Gerasimov, E. Y.; Sorokin, A. M.; Bukhtiyarov, V. I. Comparative XPS study of interaction of model and real Pt/C catalysts with NO_2. *Appl. Surf. Sci.* **2018**, *428*, 972–976.

[38] Lv, C.; Hu, C.; Luo, J. H.; Liu, S.; Qiao, Y.; Zhang, Z.; Song, J. F.; Shi, Y.; Cai, J. G.; Watanabe, A. Recent advances in graphene-based humidity sensors. *Nanomaterials* **2019**, *9*, 422.

[39] Cui, B. L.; Gao, X.; Zhao, Z.; Xue, X. F.; Yang, Q. M.; Jin, J.; Wang, W.; Liang, Y.; Guo, D. L. Contactless and passive humidity measurement by using ultra-thin GO nanosheet coated SAW sensor. *Sens. Actuators A: Phys.* **2025**, *393*, 116827.

[40] Wang, Y. J.; Zhou, Y.; Ren, H.; Wang, Y. H.; Zhu, X. Y.; Guo, Y. C.; Li, X. Room-temperature and humidity-resistant trace nitrogen dioxide sensing of few-layer black phosphorus nanosheet by incorporating zinc oxide nanowire. *Anal. Chem.* **2020**, *92*, 11007–11017.

[41] Quan, W. J.; Shi, J.; Luo, H. Y.; Fan, C.; Lv, W.; Chen, X. W.; Zeng, M.; Yang, J. H.; Hu, N. T.; Su, Y. J. et al. Fully flexible mxene-based gas sensor on paper for highly sensitive room-temperature nitrogen dioxide detection. *ACS Sens.* **2023**, *8*, 103–113.

[42] Wang, Z. Y.; Gao, S.; Fei, T.; Liu, S.; Zhang, T. Construction of ZnO/SnO_2 heterostructure on reduced graphene oxide for enhanced nitrogen dioxide sensitive performances at room temperature. *ACS Sens.* **2019**, *4*, 2048–2057.

[43] Murugesh, P.; Suruttaiya Udaiyar, P.; Mani, N. Design of Ce incorporated tricobalt tetroxide Co_3O_4 sensor with boosted gas sensing performance toward nitrogen dioxide. *J. Mater. Sci.: Mater. Electron.* **2024**, *35*, 1010.

[44] Shaikh, S. K.; Ganbavle, V. V.; Inamdar, S. I.; Rajpure, K. Y. Multifunctional zinc oxide thin films for high-performance UV photodetectors and nitrogen dioxide gas sensors. *RSC Adv.* **2016**, *6*, 25641–25650.

[45] Nguyen, V. C.; Kim, K.; Kim, H. Performance optimization of nitrogen dioxide gas sensor based on Pd–AlGaN/GaN HEMTs by gate bias modulation. *Micromachines* **2021**, *12*, 400.

[46] Martin, S. J.; Ricco, A. J. Effective utilization of acoustic wave sensor responses: Simultaneous measurement of velocity and attenuation. In *Proceedings., IEEE Ultrasonics Symposium*, Montreal, Canada, 1989, pp 621–625.

[47] Song, J. N.; Xu, Z. T.; Wu, M. H.; Lu, X. L.; Yan, Z. Q.; Chen, F.; Chen, W. P. NO_2 sensing capability of Pt–Au–SnO_2 composite nanoceramics at room temperature. *Molecules* **2023**, *28*, 1759.